https://doi.org/10.5194/egusphere-2025-6226
Preprint. Discussion started: 4 January 2026

Balloon Observations Suggesting Sea Salt Injection into the Stratosphere from Hunga Tonga-Hunga Ha'apai

Hazel Vernier[1,2,13], Demilson Quintão[3], Bruno Biazon[3], Eduardo Landulfo[4], Giovanni Souza[4], V. Amanda Santos[4], J. S. Fabio Lopes[4], C.P. Alex Mendes[4], A.S. José da Matta[4,5], K. Pinheiro Damaris[6], Benoit Grosslin[7], P.M. P. Maria Jorge[8], Maria de Fátima Andrade[8,9], Neeraj Rastogi[10], Akhil Raj[11], Hongyu Liu[12,13], Mahesh Kovilakam[12], Suvarna Fadnavis[14], Frank G.Wienhold[15], Mathieu Colombier[16], D. Chris Boone[17], Gwenael Berthet[2], Nicolas Dumelie[1], Lilian Joly[1], Jean-Paul Vernier[12,13,1]

[1]Université de Reims, Champagne-Ardenne, GSMA, 51687, France
[2]Laboratoire de Physique et de Chimie de l'Environnement et de l'Espace, Orléans, 45071, France
[3]Instituto de Pesquisas Meteorológicas - IPMet – UNESP, Chácaras Bauruenses, Bauru - SP, 17048-699, Brazil
[4]Instituto de Pesquisas Energéticas e Nucleares, University of São Paulo Butantã, São Paulo - SP, 05508-000, Brazil
[5]Escola Politécnica da Universidade de São Paulo, Butantã, São Paulo - SP, 05508-010, Brazil
[6]Departamento de Engenharia Química UFSM, Camobi, Santa Maria - State of Rio Grande do Sul, 97105-340, Brazil
[7]Institut de Combustion Aérothermique Réactivité Environnement (ICARE), 45100 Orléans, France
[8]Instituto Nacional de Pesquisas Espaciais (INPE), São José dos Campos - SP, 12227-010, Brazil
[9]Instituto de Astronomia, Geofísica e Ciências Atmosféricas, São Paulo - SP, 05508-090, Brazil
[10]Physical Research Laboratory, Ahmedabad, Gujarat 380009, India
[11]India Meteorological Department, New Delhi, Delhi 110003, India
[12]NASA Langley Research Centre, Hampton, 23666, USA
[13]National Institute of Aerospace, Hampton, 23666, USA
[14]Indian Institute of Tropical Meteorology, Pune, Maharashtra 411008, India
[15]Institut für Atmosphäre und Klima, ETH Zürich, 8006, Switzerland
[16]Department of Earth and Environmental Sciences, Munich University, München, 80333 Germany
[17]Department of Chemistry, University of Waterloo, ON N2L 3G1, Canada

Correspondence to: Hazel Vernier (hazel.vernier@gmail.com)

https://doi.org/10.5194/egusphere-2025-6226
Preprint. Discussion started: 4 January 2026

Abstract.

The explosive eruption of Hunga Tonga-Hunga Ha'apai (HTHH) in January 2022 marked a historic event as one of the largest volcanic explosions in the past 140 years. Unlike typical volcanic eruptions, which primarily inject sulfur dioxide (SO_2), HTHH introduced a massive plume of marine water vapor up to an altitude of ~57 km, reaching the mesosphere.

In this study, we use balloon-borne measurements to investigate the optical, microphysical and chemical properties of the HTHH aerosol plume eight months after the eruption. The peak concentration of the Hunga plume located between 20.5-23 km was near 8-9 #/cm^3 for aerosol diameter greater than 0.3µm and scattering ratio at 940 nm near 4-5. Our balloon-based sampling and ion chromatographic analysis revealed the presence of key ions such as Na^+, K^+, NH_4^+, Ca^{2+}, Cl^-, and traces of SO_4^{2-} in the samples collected in the lower part of the HTHH plume. These findings suggest a substantial contribution of marine aerosols to the stratospheric aerosol burden.

The results suggest that the interaction between volcanic ash, water vapor, and marine aerosols led to unique chemical processes, which significantly influenced the composition and behavior of the stratospheric aerosol layer.

https://doi.org/10.5194/egusphere-2025-6226
Preprint. Discussion started: 4 January 2026

1. Introduction

The eruption of Hunga Tonga-Hunga Ha'apai (HTHH), a submarine volcano, stands out for its direct injection of a massive plume of volcanic and submarine material up to mesospheric levels, with a record-breaking altitude of ~57 km for the uppermost part of the plume (Proud et al., 2022; Khaykin et al., 2022). Unlike typical volcanic eruptions with a Volcanic Explosivity Index (VEI) of 6 or greater, which are known for producing long-lasting sulfate aerosols from SO_2 emissions that cool surface temperatures for years (e.g., Mt. Pinatubo, Parker et al., 1996), the HTHH eruption injected a modest amount of SO_2 (~0.42 Tg) into the atmosphere (Millán et al., 2022). In addition, it introduced a substantial quantity of water vapor (146 ± 5 Tg), accounting for approximately 10% of the total stratospheric water vapor burden (Millán et al., 2022; Sellitto et al., 2022).

Satellite observations using the Aura Microwave Limb Sounder (MLS) documented this unprecedented water vapor injection (Millán et al., 2022). The abundant water vapor accelerated the transformation of SO_2 into sulfate aerosols, causing the plume to descend to 24-26 km within three weeks due to radiative cooling (Sellitto et al., 2022; Legras et al., 2022). Studies suggest that the injected H_2O vapor may have halved the lifetime of SO_2 by accelerating its conversion to sulfate aerosols (Zhu et al., 2022; Asher et al., 2023).

Early measurements from ground-based lidar and balloon-borne observations from Reunion Island documented unprecedented aerosol characteristics, including height, backscatter, and extinction coefficients, surpassing those observed since the Mt. Pinatubo eruption in 1991 (Asher et al., 2023; Baron et al., 2023). The abundant water vapor from HTHH also triggered chlorine activation, leading to rapid ozone depletion observed through balloon-borne measurements (Evan et al., 2023).

Months following the eruption, satellite observations revealed a mid-stratospheric volcanic aerosol layer and a distinct H_2O vapor layer positioned slightly above the aerosol layer at ~26 km (Schoeberl et al., 2022). The H_2O vapor layer displayed a slow ascent (~0.044 km/day) driven by the Brewer-Dobson circulation, while the aerosol layer descended due to gravitational settling of particles with an estimated diameter of ~1.2 μm (Schoeberl et al., 2022; Legras et al., 2022).

https://doi.org/10.5194/egusphere-2025-6226
Preprint. Discussion started: 4 January 2026

The HTHH eruption presents a new paradigm for volcanic aerosol research due to its unprecedented water vapor injection and unique aerosol characteristics. The warming effect of water vapor may have contributed to surpassing the Earth's average temperature increase of 1.5°C above pre-industrial levels, a critical threshold outlined in the Paris Agreement (Jenkins et al., 2023). However, recent radiative forcing estimates suggest a net cooling effect due to the dominance of aerosol-induced cooling (Schoeberl et al., 2023; Zhu et al., 2022; Sellitto et al., 2022).

We investigated the impacts of HTHH on stratospheric aerosol burden using the Global Satellite-based Stratospheric Aerosol Climatology (GloSSAC), a dataset designed to provide a cohesive time series of stratospheric aerosol properties for chemistry and climate models (Thomason et al., 2018). Figure 1 shows the temporal evolution of Stratospheric Aerosol Optical Depth (SAOD) from GloSSAC between 60° S and 60° N. The full names, eruption dates, locations, injection altitudes, Volcanic Explosivity Index (VEI), and SO_2 injection amounts corresponding to the volcanoes' names abbreviated in Figure 1, are provided in Table 1.

Figure 1a illustrates that both the Raikoke and Hunga eruptions resulted in the largest increases of SAOD since the Mount Pinatubo eruption in June 1991. We note that the SAOD for this comparison was calculated from the tropopause to 40 km, not from the 380 K isentropic level (Khaykin et al., 2022). Given that the Hunga plume was injected directly into the stratosphere, while a significant portion of the Raikoke plume remained confined to the lowermost stratosphere (between the tropopause to 380 K), the overall SAOD values for both eruptions appear similar in these calculations. Therefore, the Hunga eruption did not produce significantly larger SAOD (calculated over the full tropopause-to-40 km column) than Raikoke, contrary to previous suggestions calculating the SAOD from 380 K (Khaykin et al., 2022).

https://doi.org/10.5194/egusphere-2025-6226
Preprint. Discussion started: 4 January 2026

123 ***Table 1.*** *Summary of high-magnitude volcanic eruptions corresponding to their SO_2 injections in*
124 *the stratosphere.*

Abbreviation	Full name	Erupted on	Lat, Lon	Injection altitude (km)	VEI	Amount of SO_2 injected (Tg)
El	El Chinchon	03/28/1982	17.3º N, 93.2° W	~31	5	7.5
Pi	Pinatubo	06/15/1991	15.14º N, 20.3°E	~18-25	6	20
Ka	Kasatochi	08/07/2008	52.17º N, 175.5º W	14.5-16.5	3- 4	0.9
Sa	Sarychev	06/11/2009	48º N, 153.2º E	15	4	0.9
Na	Nabro	06/12/2011	13.3º N, 41.7º E	21	4	1.65
Ca	Calbuco	04/22/2015	41.3º S, 72.6º W	~15-22	4	0.35
Ra	Raikoke	06/22/2019	48.2º N, 153.2ºE	~13-17	4	1.5
HTHH	HTHH	01/15/2022	20.5º S, 175.3º W	57	5-6	0.45

125

126

https://doi.org/10.5194/egusphere-2025-6226
Preprint. Discussion started: 4 January 2026

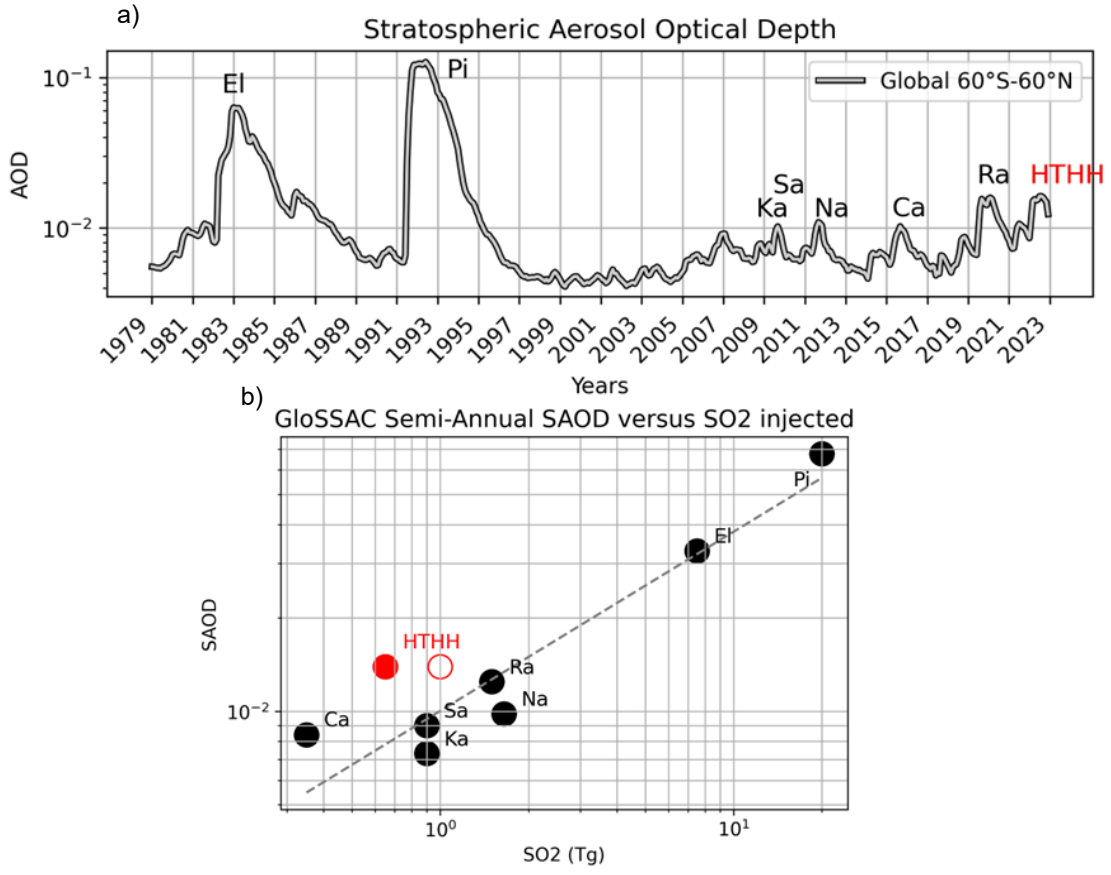

Figure 1. *(a) Quasi-global [60˚N-60˚S] Stratospheric Aerosol Optical Depth (SAOD) from the Global Satellite-based Stratospheric Aerosol Climatology (GloSSAC). (b) Semi-Annual mean SAOD and SO_2 injected by the most significant volcanic eruptions of the last 35 years. The filled red circle for HTHH corresponds to early SO_2 injected estimates (Carn et al., 2022) and the unfilled red circle to the revised estimates.*

Explosive volcanic eruptions inject SO_2 into the stratosphere, where it undergoes oxidation and nucleation, transforming into sulfate aerosols (Robock, 2000). These aerosols play a crucial role in Earth's radiative budget by reducing incoming shortwave radiation reaching the surface while absorbing near-infrared radiation and trapping outgoing longwave radiation. This combined effect leads to cooler surface temperatures and a warmer stratosphere (Robock, 2000). Furthermore, the altered radiative budget can trigger a cascade of global climate effects, including a suppressed global water cycle (Robock, 2000; Zuo et al., 2022), anomalous winter warming over Eurasia (Robock, 2000; Stenchikov et al., 2002), El Niño-like sea surface

https://doi.org/10.5194/egusphere-2025-6226
Preprint. Discussion started: 4 January 2026

temperature responses (Zuo et al., 2018; Sun et al., 2019), and a weakening of monsoon circulation. These findings highlight the complex interplay between volcanic eruptions, aerosol formation, and global climate dynamics.

To investigate the link between volcanic sulfur dioxide (SO_2) injections and their impact on stratospheric aerosol burden over the past four decades, we used data from the GloSSAC database (Kovilakam et al., 2022), since sulfate aerosols formed from volcanic SO_2 are considered the main driver of Stratospheric Aerosol Optical Depth (SAOD) and subsequent radiative and climate impacts. Figure 1b presents a scatter plot illustrating the relationship between the semi-annual sulfate SAOD (sSAOD) following major eruptions and the corresponding volcanic SO_2 injection. sSAOD was calculated by averaging SAOD data for the first 6 months after each eruption.

The HTHH eruption stands out (filled red circle). Despite injecting a relatively modest amount of SO_2 (~ 0.42 Tg) (Carn et al., 2022), it produced a significantly lower sSAOD than moderate eruptions observed since the late 2000s (Fig. 1b). For instance, the Raikoke eruption in 2019 injected about 1.5 Tg SO_2 but resulted in an sSAOD of 0.012, whereas HTHH, with its lower SO_2 injection, produced an sSAOD 16 % higher. Compared to the two largest eruptions (8 Tg for El Chichón and 20 Tg for Mt. Pinatubo) with direct stratospheric injection, the HTHH eruption exhibited a remarkably low SO_2/sSAOD ratio.

The effect of high water vapor (H_2O) on the plume evolution likely halved the lifetime of SO_2 (Zhu et al., 2022) by producing additional OH radicals for the oxidation reaction, though with relatively limited impact on the resulting maximum SAOD. The unusually high sSAOD could be partially attributed to enhanced extinction caused by water vapor-induced swelling of existing aerosols (Asher et al., 2023). While initial plume analysis revealed a 30 % increase in particle size likely caused by the high H_2O content (Asher et al., 2023), this effect likely diminished over time as the water vapor dispersed.

Further evidence from new aerosol/SO_2 retrievals using the TROPOMI instrument on Sentinel 5P (Sellitto et al., 2024) indicates that a significant fraction of sulfate (0.6 Tg) was already present in the plume two days after the eruption on January 17th, coexisting with ~ 0.5 Tg of SO_2,

https://doi.org/10.5194/egusphere-2025-6226
Preprint. Discussion started: 4 January 2026

similar to previous estimates (Carn et al., 2022). Therefore, unaccounted sulfate production within the early eruptive column could contribute to the unusual sSAOD observed and could indicate that the initial SO_2 injection was largely underestimated. Figure 1b shows that the new SO_2 estimates (unfilled red circle) align HTHH better with the expected behavior of other eruptions.

The HTHH eruption resulted in distinct aerosol particle properties in two layers: near the tropopause and in the mid-stratosphere (Kahn et al., 2024). The Multi-angle Imaging SpectroRadiometer (MISR) instrument on NASA's Terra satellite detected only spherical, non-light-absorbing particles for a week. Near-tropopause particles maintained relatively constant sizes, while mid-stratosphere particles were smaller but experienced growth downwind (Kahn et al., 2024). Despite depolarization measurements from CALIOP suggesting that aspherical particles inside the plume quickly vanished within a week after the eruption (Duchamp et al., 2025), the influence of the marine environment on the final aerosol composition remains unclear.

To study this unprecedented volcanic event, the Brazil Volcano (BraVo) project was launched to address these questions. Section 2 describes the balloon measurements conducted during the BraVo campaign. Section 3 shows the results of the Ion Chromatography (IC) analysis of the samples collected inside the Hunga plume on 8/12/2022. The interpretation of the results is discussed in Section 4, preceding the Conclusion.

2. BraVo campaign

2.1. Campaign description

The BraVo campaign deployed a suite of balloon-borne sensors in Bauru, São Paulo state (22.36° S, 49.03° W), Brazil, to investigate the physical, chemical, optical, and microphysical properties of the HTHH aerosol layer in August 2022. Ground-based lidar measurements conducted in both São Paulo and Bauru (approximately 400 km to the west of São Paulo) consistently detected a mid-stratospheric aerosol layer between 17 and 25 km throughout August 2022. Figure 2 presents the latitudinal Scattering Ratio (SR) cross-sections from the Cloud Aerosol Lidar with Orthogonal Depolarization (CALIOP) onboard the Cloud Aerosol Lidar and Infrared Pathfinder Satellite

https://doi.org/10.5194/egusphere-2025-6226
Preprint. Discussion started: 4 January 2026

Observations (CALIPSO) for the first and second halves of August (Fig. 2a and 2b), together with zonal-mean SR profiles averaged between 21° S and 23° S and the mean SR profiles retrieved on 3 and 6 August from the ground-based lidar in Bauru.

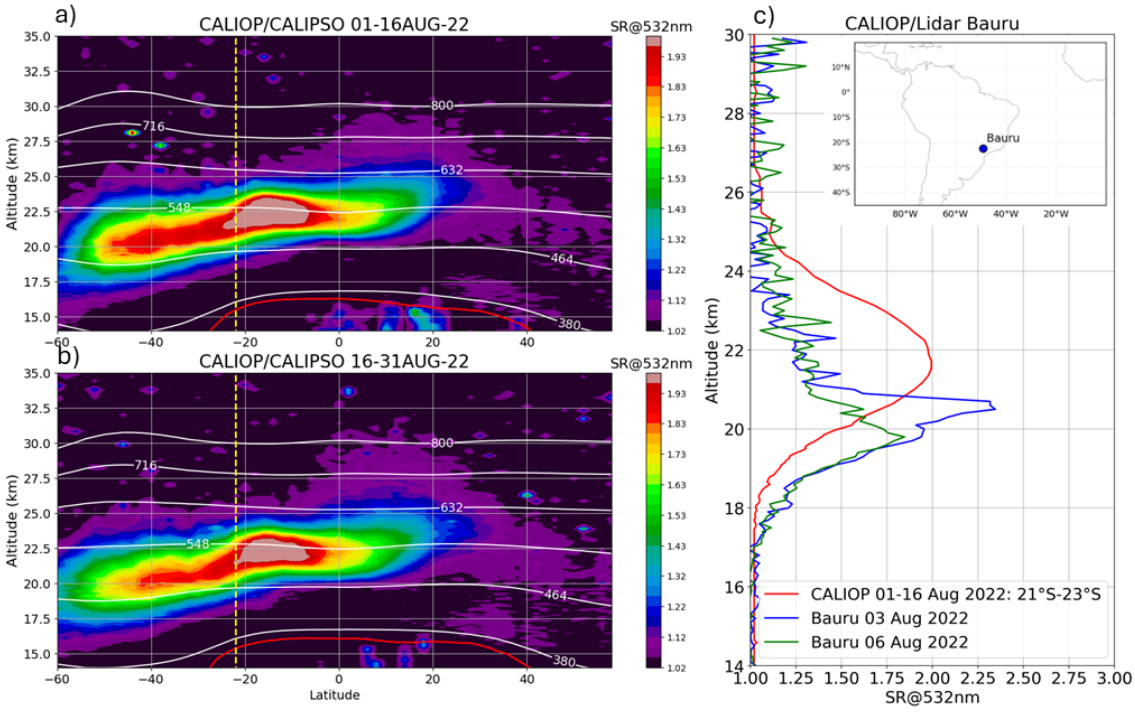

Figure 2. *Scattering Ratio (SR) cross-sections derived from 16 days of CALIOP/CALIPSO observations between 01-16 August (a) and 16-31 August (b) 2022. The yellow dashed line denotes the latitude of Bauru. (c) SR profiles from a ground-based lidar operated from Bauru during the BraVo campaign on 3 and 6 August 2022, compared with CALIOP SR profiles averaged between 21˚S and 23˚S around Bauru. Due to instrumental noise, data in the South Atlantic Anomaly have been removed.*

The HTHH plume observed by CALIOP appears to be shifted upward by 1-2km in altitude compared to the ground-based measurements, which indicate that the plume was still not homogeneously dispersed 8 months after the eruption. In addition, CALIOP cross-sections suggest significant changes in the vertical structure of the plume near 20˚S with a higher and thicker plume located toward the tropics, while the plume height and strength decrease toward southern mid-latitudes. It is important to note that CALIPSO data were unavailable

https://doi.org/10.5194/egusphere-2025-6226
Preprint. Discussion started: 4 January 2026

over Brazil due to interference from the South Atlantic Anomaly (SAA), and a direct comparison is therefore not possible. In addition to the ground-based lidar observations from Bauru, a series of balloon flights was conducted in August 2022 as part of the BraVo project.

2.2. Optical and Microphysical measurements inside the HTHH plume

Table. 2 describes the dates of the balloon flights and the aerosol instruments used during the BraVo campaigns in August 2022. One flight on 08/12 was co-located with a sunrise occultation from the Stratospheric Aerosol and Gas Experiment (SAGE) III/ISS (see Supplementary Materials). Further descriptions of the balloon-borne instruments are provided below.

Table 2. *List of balloon flights, launch time, and instruments used in August 2022 during the BraVo campaign.*

Flight_ID	Launch Time (UTC)	POPC	COBALD	Sampler	SAGE III/ISS
20220807_BRU_BraVo_08	**6h30m**	**x**	**x**		
20220812_BRU_BraVo_09	**6h30m**	**x**	**x**		**x**
20220816_BRU_BraVo_10	**18h30m**			**x**	
20220820_BRU_BraVo_11	**6h30m**	**x**	**x**		

A lightweight balloon-borne Profiling Optical Particle Counter (POPC) (<2kg) was developed from the Particle Plus 9301OEM instrument for weather balloon applications (Dumelié et al., 2024). This POPC measures aerosol concentration profiles at 30 diameters (radii) between 0.3-10 µm (0.15-5 µm) from the ground to the stratosphere. The system employs a laser diode emitting at 785 nm. As particles enter the optical chamber, the

https://doi.org/10.5194/egusphere-2025-6226
Preprint. Discussion started: 4 January 2026

scattered light at 90 degrees is amplified and converted into a voltage using a high-speed ADC (analog-to-digital converter), providing a digital measurement of the pulse height. The data are then calibrated in the laboratory using PSL spheres for size channels to be defined and raw data transformed into aerosol counts in the 30 size bins available. The scattering efficiency of PSL, sulfate and sea salt (Fig. S1) shows that the size thresholds of the POPC measurements need to be corrected.

COBALD is a lightweight (540g) instrument that consists of two high-power light-emitting diodes (LEDs) emitting approximately 500 mW of optical power at wavelengths of 470 and 940 nm, respectively. The backscattered light from molecules, aerosols, or ice particles is recorded by a silicon photodiode using phase-sensitive detection. The precision of the backscatter ratio measurements is better than 1% in the UTLS region (Vernier et al., 2015). Figure 3 presents total aerosol concentration profiles alongside the scattering ratio-minus one for three flights conducted on August 7th, 12th, and 20th. Aerosol concentration peaks within the Hunga plume range from 8 to 9 #/cm³ at altitudes between 20.5 and 23 km. The corresponding variations in scattering ratio within the stratosphere show good qualitative agreement with the aerosol concentration profiles, demonstrating consistency between these independent measurements. The 3 flights show that the HTHH plume was still not homogeneous. Additional comparisons between COBALD, POPC and SAGE III/ISS (Fig. S2) for the flight on 08/12 indicate relative differences within +/- 50% for measured and calculated extinction coefficients in the HTHH plume.

https://doi.org/10.5194/egusphere-2025-6226
Preprint. Discussion started: 4 January 2026

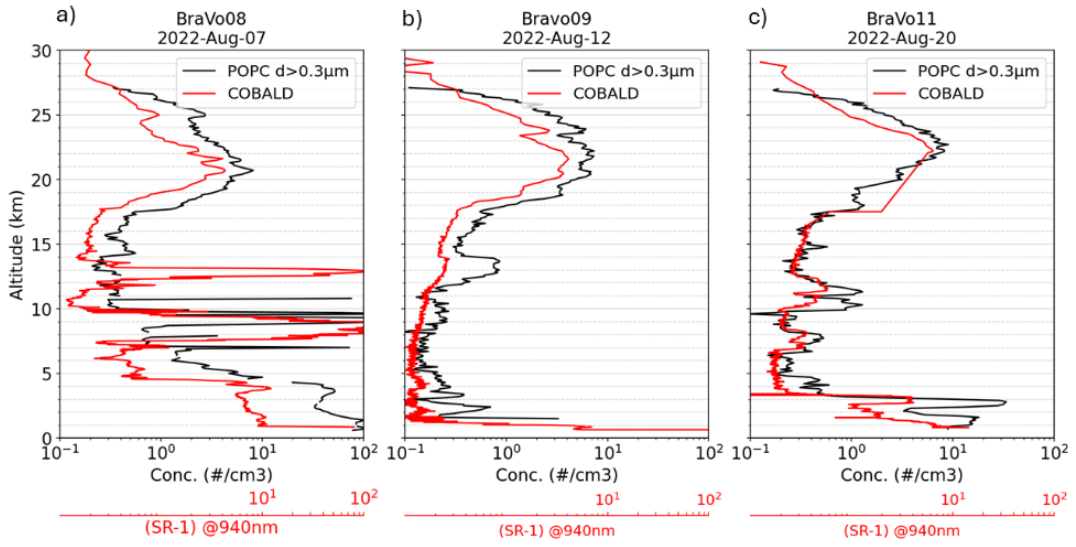

Figure 3. *POPC aerosol profiles (radius > 0.15 µm) for August 7th, 12th, and 20th. COBALD aerosol backscatter ratio-minus-1 profiles at 940 nm for August 7th and 12th are also shown.*

2.3. Chemical Sampler

The CHEM filter Sampler is a sampling device that captures aerosol particles on filters for offline chemical analysis. It was previously used to study organic aerosols from the troposphere to the stratosphere using Orbitrap through offline analysis (Benoit et al., 2023, 2024). The sampler has eight filter cartridges that hold individual filters. Figure 4d provides a quick overview of the sampler's working principle. The eight filters located in each position (marked “P”) makes it possible to perform time-resolved sampling under user control. The rotation of magnets allows the opening and closing of the valves through a rotating wheel so that only one valve is opened at a time. In the example provided (Figure 4d), only position 2 had the valve opened and sampled aerosols while the others remained closed. The CHEM filter sampler was adapted for balloon flight applications using an Imet radiosonde and a Raspberry PI system to control the sampling altitudes along the flight altitudes. Only one sampler flight could be performed in August 2022. Figure 4 (a,b,c) shows the time evolution of the different parameters monitored along this flight (GPS altitude, sampler flow, position number (Cur_pos), internal temperature). The controlled position

https://doi.org/10.5194/egusphere-2025-6226
Preprint. Discussion started: 4 January 2026

numbers along the flight are also annotated on Fig. 4a, 4b and 4c using "P" and a number as a suffix.

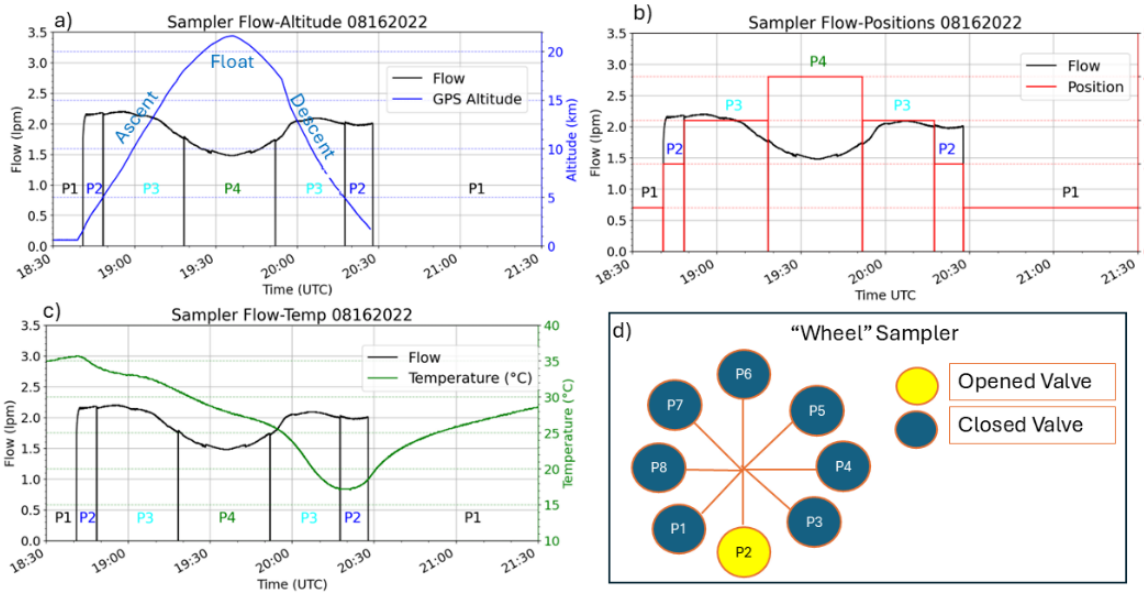

Figure 4. *Time evolution of (a) GPS altitude and sampler flow rate, (b) sampler position and flow rate, and (c) internal temperature and flow rate during the sampler flight on 16 August 2022. Black Vertical lines indicate the boundaries between sampling positions when the pump is turned off and the system moves to another position (d) Schematic of the "Wheel" sampler concept, showing opened and closed valves during sampling, with an example of sampling at position P2. During this flight Position 6,7,8 was not used for sampling and Position 1 remained open when the instrument was on but without the pump on (Standby position). The total volume of air on position 2,3 and 4 was 36 L, 113 L, and 53 L.*

The balloon system was equipped with a radio-controlled valve to extend aerosol sampling in the lower stratosphere (Vernier et al., 2018). The flight trajectory included a controlled reduction in ascent rate near 19.0 km, followed by a slow climb to a peak altitude of 21.6 km before descent (Fig. 4a). This maneuver allowed an extended float period for the sampler to remain within the plume for approximately 40 min, significantly longer than conventional balloon flights (~15min). The extended sampling time maximized aerosol collection, allowing additional mass to be collected. The internal temperature of the sampler air flow ranged between 17 and 35 °C during the flight (Fig. 4c) and remained below 36 °C up to the recovery before the samplers were positioned into a dry to minimize aerosol loss and chemical reactions.

https://doi.org/10.5194/egusphere-2025-6226
Preprint. Discussion started: 4 January 2026

Due to weather and logistical constraints, only a single flight was conducted using this enhanced system. The radio-controlled valve was critical for optimizing the flight path and sampling duration, thereby enhancing the quality and reliability of the collected data for the subsequent chemical analysis described herein. The Ion Chromatography (IC) technique used to analyze the samples is presented in the next section.

2.4. Offline Analysis and Ion Chromatography

Water-soluble inorganic species (WSIS), including K^+, Na^+, Mg^{2+}, Ca^{2+}, NH_4^+, Cl^-, F^-, Br^-, NO_2^-, NO_3^-, and SO_4^{2-}, were analyzed using two Dionex Integrion High-Performance Ion Chromatographs (HPIC) with conductivity detection. Anions were separated using an AS-18-FAST-4 µm, 2 × 150 mm column with a KOH gradient eluent over 25 minutes: 10 mM from 0 to 6 minutes, increasing to 60 mM from 6 to 15 minutes, and maintained at 60 mM from 15 to 25 minutes. Cations were separated using a CS-12A, 4 × 250 mm column with a Methyl Sulfonic Acid gradient eluent over 25 minutes: 10 mM from 0 to 6 minutes, increasing to 35 mM from 6 to 15 minutes, and maintained at 35 mM from 15 to 25 minutes.

Ultrapure water for dilutions, extractions, and mobile phase preparation was generated using an EQ7000 Millipore water purification system (Resistivity ≥ 18.2 MΩ·cm). Calibration standards were prepared from high-purity analytical grade solutions from Merck (NH_4Cl, $CaCO_3$, KNO_3, $Mg(NO_3)_2$, and $NaNO_3$ for cations; NaCl, $NaNO_3$, NaBr, $NaNO_2$, and Na_2SO_4 for anions). Working standards with concentrations of 1, 5, 10, 50, and 100 µg/L (ppb) were prepared and injected into the instrument (250 µL sampling loop) to establish a calibration range.

The ultrapure water was pre-checked for potential cation and anion contamination before sample analysis. The detection limits (LODs) for each ion were determined by injecting 15 ultrapure water blanks from the EQ7000 system, with LODs calculated as the average blank value plus three times the standard deviation (LOD = $\bar{x}$ + 3s). The LOD values for each ion are provided in Table 3.

https://doi.org/10.5194/egusphere-2025-6226
Preprint. Discussion started: 4 January 2026

2.5. IC Data Analysis and Error Calculation of IC

Filters from positions P 1-P 5 were extracted and analyzed by ion chromatography. Each extract was injected three times to assess reproducibility. For each position (P1–P4), the two injection results with the smallest difference were selected to minimize the impact of potential outliers. The average, standard deviation, and percent relative standard deviation (%RSD) were calculated for these selected values.

Since no collection was performed on P5, it was used as a blank. Its average and standard deviation were calculated across all three injections. To correct for the background signal, the average of the reference blank (P5) was subtracted from the average of each sample, yielding the corrected average for each sample.

The error bars for the corrected averages were determined by propagating the uncertainty from both the sample and reference blank measurements. The standard error of the mean (SEM) was calculated for the selected injections of each sample and for the reference blank. The total SEM was derived using the quadrature sum of the individual SEMs, and the error bars were reported as ±1.96 × total SEM, corresponding to a 95% confidence interval (CI).

Finally, the corrected averages and their associated error bars were multiplied by the dilution factor and divided by the volume of air filtered (in m^3) to report the final concentrations in ng/m^3.

https://doi.org/10.5194/egusphere-2025-6226
Preprint. Discussion started: 4 January 2026

3. Results

3.1. Raw mass concentrations

The raw mass concentrations of major ions, measured by ion chromatography (IC) before blank correction, are presented in Table 3. These values represent the detected mass of each ion in the samples, along with their respective Limits of Detection (LOD). We note that only one value reported was lower than the LOD for K^+ on Position 3. We observed that the ionic mass observed in each position is highly correlated as a function of ion types.

Table 3 *Raw mass concentrations of major ions at Positions 2, 3, 4, and 5 analyzed using ion chromatography (IC). Values represent raw mass concentrations (ppb or ng/mL) measured by IC before blank correction. LOD values are provided for each ion. These raw values were used to ensure transparency and avoid bias in the initial detection of ions.*

Ions	P 2 (ppb)	P 3 (ppb)	P 4 (ppb)	P 5 (ppb)	LOD (ppb)
Na^+	22.71	15.63	25.67	14.94	7.76
K^+	7.62	3.58	12.29	7.65	6.34
NH_4^+	36.81	30.58	39.32	25.75	4.05
Mg^{2+}	2.34	1.90	2.35	1.80	0.36
Ca^{2+}	20.42	27.52	33.87	15.78	13.70
F^-	11.70	17.20	24.40	14.48	3.71
Cl^-	28.27	17.04	37.95	16.12	2.91
NO_2^-	4.80	28.67	14.21	13.04	0.28
NO_3^{2-}	19.73	7.70	9.24	5.03	1.01
SO_4^{2-}	8.70	4.51	5.52	5.52	1.48

3.2. Processed Data

The processed mass concentrations of major ions, after blank correction, were derived by using the total volume of air that passed through each filter measured onboard the sampler. The total volume of air on positions 2,3 and 4 was 36 L, 113 L, and 53 L. The mass concentrations

https://doi.org/10.5194/egusphere-2025-6226
Preprint. Discussion started: 4 January 2026

reported in Table 4 are in µg/m³. These values include 95% confidence intervals (CI) and are used for the IC bar plots shown in Figure 5.

Table 4. *Processed concentrations of major ions at P 2, P 3, and P 4, with 95% confidence intervals derived from raw mass values. Concentrations represent statistically processed data derived from the raw mass values presented in Table 1. Values are blank-corrected and converted to µg/m³. The 95% confidence intervals (CI) are provided for each ion concentration. Values below the LOD or negative after blank subtraction are indicated by a dash (—). These processed values are used for further statistical analysis and graphical representation in the IC bar plots.*

Ions	**P 2 (μg/m^3)**	**P 3 (μg/m^3)**	**P 4 (μg/m^3)**
Na^+	1.29±0.47	0.04±0.13	1.21± 0.07
K^+	-	-	0.53± 0.15
NH_4^+	1.84±1.42	0.26±0.37	1.53± 0.24
Mg^{2+}	0.08± 0.02	0.01± 0.01	0.06± 0.01
Ca^{2+}	0.77±0.83	0.63± 0.18	2.05± 0.05
F^-	-	0.15±0.19	1.12± 0.48
Cl^-	2.02± 0.89	0.05± 0.38	2.47± 0.68
NO_2^-	-	0.83	0.14± 0.03
NO_3^{2-}	2.44± 0.21	0.15± 0.05	0.48± 0.1
SO_4^{2-}	0.53± 0.04	-	0.06± 0.07

Table 4 presents the processed concentrations after blank correction and conversion to µg/m³, including 95% confidence intervals. This approach allows readers to distinguish between raw detection data and statistically processed results used for further analysis.

The concentrations of major ions are visualized in Figure 5. The bar graphs illustrate the concentrations (µg/m³) of Na^+, K^+, NH_4^+, Mg^{2+}, Ca^{2+}, F^-, Cl^-, NO_2^-, NO_3^-, and SO_4^{2-} at three altitudes: Position 2 (1.6–5.0 km), Position 3 (5.0–18.1 km), and Position 4 (18.1–21.6 km).

https://doi.org/10.5194/egusphere-2025-6226
Preprint. Discussion started: 4 January 2026

Error bars represent the 95% confidence intervals for each ion concentration, indicating the reliability of the measurements.

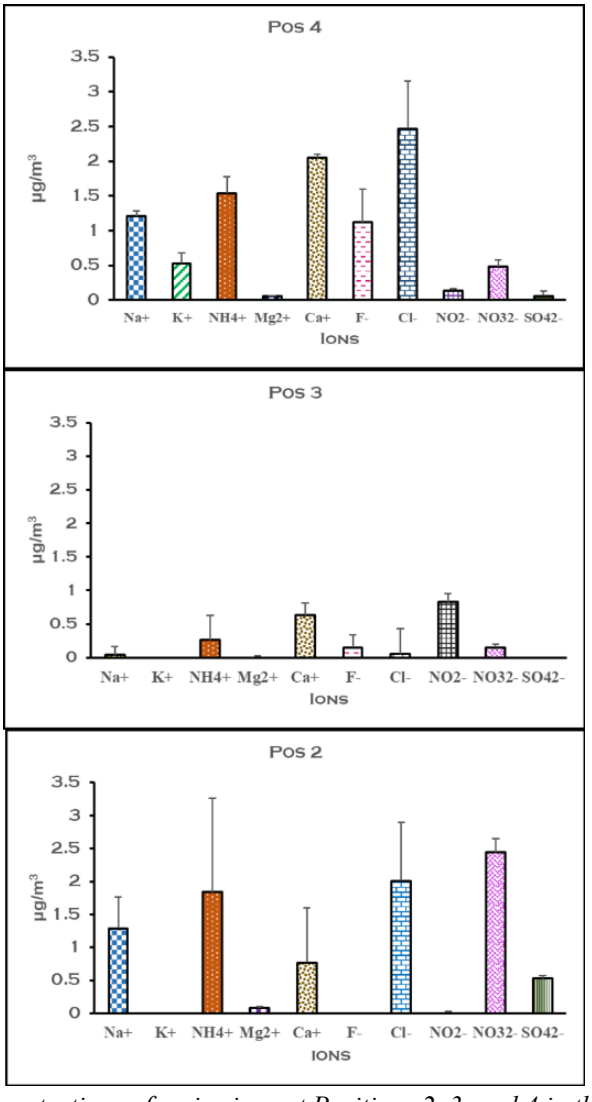

Figure 5: *Concentrations of major ions at Positions 2, 3, and 4 in the Hunga Tonga volcanic plume. The bar graphs show the concentrations (µg/m³) of* Na^+, K^+, NH_4^+, Mg^{2+}, Ca^{2+}, F^-, Cl^-, NO_2^-, NO_3^-, *and* SO_4^{2-}.

https://doi.org/10.5194/egusphere-2025-6226
Preprint. Discussion started: 4 January 2026

The concentrations of major ions at different positions are illustrated in Figure 5. The bar graphs represent the concentrations (μg/m³) of Na^+, K^+, NH_4^+, Mg^{2+}, Ca^{2+}, F^-, Cl^-, NO_2^-, NO_3^-, and SO_4^{2-} at three altitudes at Position 2 (1.6-5.0 km), Position 3 (5.0-18.1 km), and Position 4 (18.1-21.6 km). Error bars represent the 95% confidence intervals for each ion concentration, indicating the reliability of the measurements. Sodium (Na^+) and chloride (Cl^-) exhibited pronounced enhancements at Pos 4 (16–18 km), reaching concentrations of 1.21± 0.07 μg/m³ and 2.47± 0.68 μg/m³, respectively. Sulfate (SO_4^{2-}) concentrations decreased vertically, from 0.53± 0.04 μg/m³ at Pos 2 to 0.06± 0.07 μg/m³ at Pos 4. In contrast, calcium (Ca^{2+}) showed significant enrichment at Pos 4 (2.05± 0.05 μg/m³) compared to Pos 2 and Pos 3. Ammonium (NH_4^+) and nitrate (NO_3^-) dominated at Pos 2 (1.84±1.42 μg/m³ and 2.44± 0.21 μg/m³, respectively).

3.3. Molar Ratios of Major Ions

We calculated the concentrations in **μmol/m³** to further analyze the relative abundance and potential chemical interactions of these ions. The molar ratios of major ions relative to Na^+ and SO_4^{2-} at Positions 2, 3, and 4 are presented in Table 5.

Table 5. *Key molar ratios used to identify sea salt injection, volcanic ash contribution, and sulfate depletion*[*]

Ratios	**Interpretation**	**Seawater Reference**	**Pos 2 (1.6–5 km)**	**Pos 3 (5–18.1 km)**	**Pos 4 (18.1–21.6 km)**
Na^+/Cl^-	Sea salt signature	0.86	0.98	1.23	0.76
Mg^{2+}/Na^+	Sea salt consistency	0.12	0.06	0.24	0.047
K^+/Na^+	Volcanic ash enrichment	0.02	-	-	0.26
Ca^{2+}/Na^+	Ash & crustal source	0.02	0.34	12.6	0.97
Cl^-/SO_4^{2-}	Sulfate depletion indicator	19.00	10.25	-	110.47
Ca^{2+}/SO_4^{2-}	Gypsum formation diagnostic	0.36	3.50	-	81.40

https://doi.org/10.5194/egusphere-2025-6226
Preprint. Discussion started: 4 January 2026

NO_3^- /SO_4^{2-}	Neutralization / secondary aerosol	1.00	19.10	-	142.70

Table Notes: *BDL = Below Detection Limit. Seawater reference ratios are derived from Millero et al. (2008). Measured values are presented for three altitude ranges: Pos 2 (1.6–5 km), Pos 3 (5–18.1 km), and Pos 4 (18.1–21.6 km).

3.4. Calculating Marine Enrichment Factors (EFs)

Enrichment factors (EFs) compare the ratio of an element to a reference element. Herein, we calculate the Marine Enrichment Factors (MEFs) since we study the enhancement of an element to compare to what is expected in sea water. This helps identify non-marine sources or processing. MEFs were determined using the formula:

$$MEF_{ion} = (Ion/Na^+)_{sample}/ (Ion/Na^+)_{seawater}$$

if MEF ≈ 1, the element is primarily marine-derived.

If MEF > 1, there is an additional non-marine source or enrichment.

If MEF < 1, the element is depleted relative to seawater.

MEFs were calculated following the methodology described in the supplement of Barbaro et al. (2024). MEFs were used to assess the marine contribution to aerosol composition. Table 4 shows the MEFs using the Na^+:Cl^-, Na^+:Mg^{2+}, and Na^+:SO_4^{2-} ratios from our data and comparing them to seawater ratios.

Table 6. MEFs values using Na^+:Cl^-, Na^+:Mg^{2+}, and Na^+:SO_4^{2-} ratios from our data compared to ratios in seawater*.

Ion	**Seawater (Ion/Na^+)**	**Pos 2 MEF**	**Pos 3 MEF**	**Pos 4 MEF**
Cl^-	1.16	0.87	0.70	1.14
Mg^{2+}	0.11	0.52	2.09	0.42
SO_4^{2-}	0.06	1.63	MDL	0.20

https://doi.org/10.5194/egusphere-2025-6226
Preprint. Discussion started: 4 January 2026

*MDL = Measurable Detection Limit not achieved. These MEFs quantify deviations of the measured ionic composition from seawater reference ratios. Values greater or less than 1 indicate enrichment or depletion relative to seawater

The combined ppb concentrations, molar ratios, and enrichment factors display systematic differences among Positions 2, 3, and 4. Variations occur in the relative abundances of Na^+, Cl^-, Ca^{2+}, and SO_4^{2-}, and in the magnitude of the corresponding ratios. These differences describe the vertical structure of the sampled aerosol composition. Interpretation of these differences is provided in the Discussion section below.

4. Discussion

4.1. Theoretical considerations: Sampling efficiency inside the HTHH plume

The sampler flight on 08/16 was performed without additional aerosol measurements due to weight restrictions. However, we investigate the theoretical mass that the sampler would have collected based on size distribution measurements from the POPC flights before (08/07, 08/12) and after (08/20) the sampler flight to understand the connections between the IC chemical analysis in section 3 and microphysical properties of the plume in section 2.

https://doi.org/10.5194/egusphere-2025-6226
Preprint. Discussion started: 4 January 2026

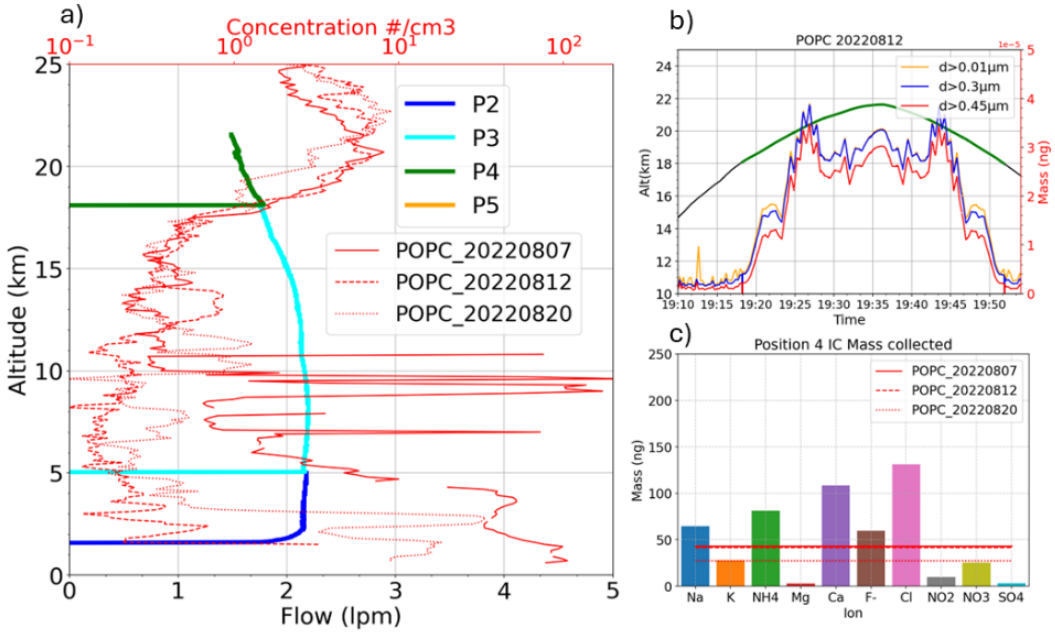

Figure 6. *(a) Vertical profile of sampler flow rate colored as a function of position number for the ascending part of the balloon flight on 08/16, along with total aerosol concentration from POPC measurements on 08/07, 08/12, and 08/20. (b) Theoretical mass collected per second ford>0.01 µm, 0.3 µm, and 0.45 µm along the sampler flight using sampler flow rate on 08/16 and POPC size distribution data on 08/07, 08/12, and 08/20. The green portion of the GPS time series corresponds to the time and altitude at which sampling was done on position 4 (c). Total oonic mass on position (colored bars) and total theoretical mass collected on position 4 derived from the 3 POPC flights (horizontal red lines),*

The theoretical mass of aerosols collected during flights was derived using a multi-step approach. First, a log-normal distribution was fitted to the number concentration data obtained from the POPC. An assumed aerosol density (d=1.8kg/L) consistent with sulfate aerosol was then used to convert number concentrations to mass concentrations along the flight path. Finally, the mass concentration data were interpolated along the sampler flight path, and the theoretical mass collected was calculated based on the flow rate associated with each sampling position. Further details are provided in the Supplemental Materials (S3).

Figure 6a shows the sampler flight traversed the lower region of the HTHH plume where aerosol concentrations were estimated between 1–10 particles cm^{-3} from the POPC flights before and after 08/16. Variations in aerosol concentrations in the boundary layer and upper troposphere were

https://doi.org/10.5194/egusphere-2025-6226
Preprint. Discussion started: 4 January 2026

observed across the three flights, likely due to changing weather conditions and contributions from intermittent sources, such as forest fires in the Amazon region.

The theoretical mass derived from POPC data is near 42–43 ng for the first two flights and 27 ng for the flight on 20 August. In comparison, the total ion mass measured by IC was 513 ng, exceeding theoretical estimates largely (Fig. 6c). This difference may reflect variability in aerosol size distributions not fully captured by POPC or a potential source of contamination in the IC data. Importantly, the detected ion concentrations were consistently above the instrument's Limit of Detection (LOD), confirming the high sensitivity and reliability of the IC measurements.

4.2. Na^+:Cl^- Ratios and Marine Source Identification

Ion chromatography analysis of the aerosol samples collected post-eruption reveals distinct Na^+:Cl^- molar ratios consistent with marine origins and subsequent chemical processing.

At Position 2 (1.6–5 km altitude), the Na^+:Cl^- ratio of 0.98 suggests a predominantly marine signature. While this altitude range represents the lower free or middle troposphere rather than the marine boundary layer, the presence of sea salt aerosols at these altitudes is consistent with observations of long-range transport and convective lofting of marine aerosols into the upper troposphere (Murphy et al., 2018). Murphy et al. (2018) documented the global distribution of sea salt aerosols, including their presence at altitudes up to 12 km, particularly in regions influenced by strong convective activity and cyclonic systems.

At Position 3 (5–18.1 km), the elevated Na^+:Cl^- ratio (1.23) indicates chloride depletion via acid displacement reactions, such as HCl volatilization or sulfate-driven Cl^- loss, as previously observed in volcanic plumes interacting with acidic gases (Zhao et al., 1996; Mather et al., 2003). This process occurs when SO_2 is oxidized to sulfate, increasing aerosol acidity and lowering the Henry's law constant (He*) of HCl*, which promotes its volatilization from fine particles (Allen et al., 2000). As a result, fine aerosols exhibit elevated Na^+:Cl^- ratios due to the loss of Cl^- as gaseous HCl.

Similarly, Position 4 (18.1–21.6 km) exhibits a reduced Na^+:Cl^- ratio (0.76), likely reflecting partial Cl^- scavenging during ascent. Allen et al. (2000) observed that volatilized HCl can be subsequently scavenged by coarser particles, leading to lower Na^+:Cl^- ratios in those particles.

https://doi.org/10.5194/egusphere-2025-6226
Preprint. Discussion started: 4 January 2026

These deviations from seawater stoichiometry demonstrate progressive chemical modification of marine aerosols with altitude, driven by interactions with volcanic acids and sulfates.

4.3. Stratospheric Sea Salt Signature

The near-marine Na^+/Cl^- ratio (0.76) at Position 4 confirms the presence of minimally processed sea salt aerosols at 18.1–21.6 km altitude (Table 5). This ratio deviates only slightly from seawater (0.86), indicating rapid vertical transport of marine material without significant fractionation. Such efficient injection is characteristic of submarine eruptions with high water-to-magma interaction ratios, as modeled for Hunga Tonga's explosive phase (Colombier et al., 2023). Comparable stratospheric sea salt enrichments have been documented during large phreatomagmatic eruptions, including Pinatubo (1991) and Holuhraun (2014–2015) (Tabazadeh et al., 2002; Ilyinskaya et al., 2017). However, Hunga Tonga's Na^+ concentrations (0.056 µmol/m³) exceed prior measurements due to its exceptional eruptive water flux.

4.4. Calcium-Rich Ash and Sulfate Uptake Mechanisms

Non-sea-salt species, particularly Ca^{2+} and SO_4^{2-}, exhibit marked deviations from seawater composition. Elevated Ca^{2+}/Na^+ ratios ($\gg 1$) and Ca^{2+}/SO_4^{2-} ratios confirm the dominance of Ca-bearing volcanic ash in the aerosol mixture. The extreme Ca/SO_4 ratio ($\gg 1$) quantitatively supports heterogeneous sulfate consumption via gypsum formation ($Ca^{2+} + SO_4^{2-} \rightarrow CaSO_4\downarrow$), a process favored under Ca-rich, sulfate-limited conditions (Stumm & Morgan, 2012). Insoluble $CaSO_4$ precipitation removes soluble SO_4^{2-} from the aerosol phase, directly explaining the anomalously low sulfate concentrations measured in IC analyses. This mechanism aligns with experimental studies of ash-sulfate interactions (Ayris & Delmelle, 2012) and satellite retrievals of fine ash aggregation in the Hunga Tonga plume (Gupta et al., 2022).

4.5. Marine Enrichment Factors (MEFs) and Source Apportionment

MEF calculations relative to seawater compositions (Nozaki, 2010) corroborate source contributions:

https://doi.org/10.5194/egusphere-2025-6226
Preprint. Discussion started: 4 January 2026

Position 2: Cl^- MEF (0.87) and Mg^{2+} MEF (0.52) near unity confirm marine dominance. Elevated SO_4^{2-} MEF (1.65) reflects magmatic SO_2 oxidation products (Sellito et al., 2024).

Position 3: Reduced Cl^- MEF (0.70) validates acid-mediated chloride loss. Absence of detectable SO_4^{2-} (MEF = 0.00) suggests localized sulfate depletion via $CaSO_4$ formation or measurement artifacts.

Position 4: Near-unit Cl^- MEF (1.14) reaffirms marine chloride sourcing, while suppressed Mg^{2+} (0.42) and SO_4^{2-} (0.20) MEFs indicate mixing with Ca-rich ash or sulfate scavenging.

4.6. Implications for Stratospheric Aerosol Composition

The combined Na^+:Cl^-, Ca^{2+}/SO_4^{2-}, and MEF data provide conclusive evidence for co-injection of sea salt aerosols and Ca-rich ash into the stratosphere. Observed sulfate depletion correlates directly with Ca^{2+} availability, validating gypsum precipitation as the primary sink for SO_4^{2-}. Chloride loss patterns align quantitatively with acid-displacement kinetics parameterized in volcanic plume models (Mather et al., 2003).

4.7. Factors Driving Low Sulfate Concentrations

The anomalously low SO_4^{2-} levels detected in IC analyses at Position 4 (18.1–21.6 km) can be explained by the following mechanisms, which also help reconcile discrepancies with satellite observations from ACE-FTS (Fig. S4).

Heterogeneous Gypsum Formation: The high Ca^{2+}/SO_4^{2-} ratios ($\gg$1) at Position 4 indicate preferential sulfate removal via $CaSO_4$ precipitation, reducing aqueous-phase SO_4^{2-} concentrations by >90% in ash-rich regions (Zhao et al., 1996; Colombier et al., 2023). This process leads to the formation of insoluble $CaSO_4$ aggregates, which are not detected by standard IC protocols optimized for soluble aerosols. Satellite observations, which measure total sulfate (including insoluble forms), may therefore show higher concentrations than IC analyses.

Rapid SO_2 Oxidation and Aqueous-Phase Reactions: Unlike typical volcanic eruptions, the Hunga Tonga event injected massive amounts of water vapor into the stratosphere (Millán et al., 2022), creating conditions favorable for rapid SO_2 oxidation and sulfate formation (Eatough et

https://doi.org/10.5194/egusphere-2025-6226
Preprint. Discussion started: 4 January 2026

al., 1994; Farlow et al., 1981). However, the resulting sulfate may have precipitated as insoluble $CaSO_4$ or been scavenged by ash particles, reducing the soluble sulfate fraction detected by IC. The high-H_2O content would accelerate aqueous-phase reactions, but the presence of Ca-rich ash would promote gypsum formation, removing soluble sulfate from the aerosol phase.

Acid Displacement and Chloride Scavenging: Volcanic HCl and H_2SO_4 react with sea salt particles, releasing Cl^- as HCl(g) and displacing SO_4^{2-} adsorption sites (Finlayson-Pitts & Pitts, 2000). This process can lead to low soluble sulfate concentrations in IC analyses, even if total sulfate (including insoluble forms) remains high.

Neutralization by Background Ammonia: As the plume ages, neutralization of acidic species by background ammonia can further reduce soluble sulfate levels (Allen et al., 2000). This process is highly variable and depends on local atmospheric conditions, potentially leading to underestimation of sulfate in IC analyses if neutralization products (e.g., $(NH_4)_2SO_4$) are not fully dissolved or detected. The neutralization of acidic species by background ammonia may contribute to the low soluble sulfate concentrations observed in our IC analyses. At Position 2 (1.6–5 km), the concentration of NH_4^+ (1.84 ± 1.42 µg/m³) is significantly higher than at Position 3 (0.26 ± 0.37 µg/m³) and Position 4 (1.53 ± 0.24 µg/m³) (Table 2). This suggests that ammonia neutralization of acidic sulfate species (e.g., H_2SO_4) may have occurred more extensively at lower altitudes, where NH_4^+ concentrations are elevated.

The formation of ammonium sulfate ($(NH_4)_2SO_4$) or ammonium bisulfate (NH_4HSO_4) through neutralization reactions can reduce the concentration of soluble SO_4^{2-} in the aerosol phase. For example, at Position 2, where NH_4^+ levels are highest, the SO_4^{2-} concentration is 0.53 ± 0.04 µg/m³, while at Position 3, where NH_4^+ levels are lower, SO_4^{2-} is below the detection limit (Table 2). This pattern supports the hypothesis that ammonia neutralization may have contributed to the underestimation of soluble sulfate in our IC analyses, particularly if the resulting ammonium sulfate particles were not fully dissolved or detected.

This process is highly variable and depends on local atmospheric conditions, including the availability of ammonia and the degree of mixing within the plume (Allen et al., 2000). The variability in NH_4^+ and SO_4^{2-} concentrations across altitudes suggests that neutralization

https://doi.org/10.5194/egusphere-2025-6226
Preprint. Discussion started: 4 January 2026

reactions played a role in modifying the soluble sulfate content of the aerosols, particularly in the lower altitudes where NH_4^+ was more abundant.

Analytical Limitations of IC: Insoluble $CaSO_4$ aggregates (>1 μm) and other sulfate-containing particles may evade detection by IC, which is optimized for submicron soluble aerosols. Satellite remote sensing, however, can detect the total sulfate burden (including insoluble and gas-phase SO_2), leading to apparent discrepancies between the two methods.

5. Summary and Conclusion

The HTHH plume produced unusual SAOD compared to early estimates of SO_2 emitted from satellite observations. Recent studies have suggested that those initial estimates could have been underestimated due to the rapidly formed sulfate aerosol in the very early stage of the eruption (Sellitto et al., 2024). Furthermore, microphysical calculations indicated that nucleation processes in the moist plume may have led to the production of aerosols with effective radius near 0.4μm with higher scattering efficiency than smaller aerosols produced by traditional medium size volcanic eruptions and may explain this unusual SAOD (Li et al., 2024).

This eruption injected an exceptional mass of seawater directly into the stratosphere, providing a unique opportunity to examine the impact of such events on stratospheric aerosols. Utilizing balloon-borne data from the BraVo campaign in Brazil, we analyzed the optical, microphysical, properties and chemical composition of the plume. Our analysis shows consistency between POPC, COBALD and SAGE III/ISS regarding the vertical structure of the HTHH plume and the derived extinction coefficients. The chemical analysis demonstrates that sea salt aerosols played a significant role in the composition and behavior of the stratospheric plume, alongside magmatic SO_2 and fine ash. The efficient lofting of sea salts and their interaction with volcanic ash (e.g., gypsum formation) may have contributed to the rapid removal of coarse particles and the persistent presence of fine aerosols in the stratosphere. These processes are likely characteristic of large-scale submarine eruptions and warrant further investigation to improve our understanding of their radiative and climatic effects (Zhu et al., 2023; Sellito et al., 2024).

https://doi.org/10.5194/egusphere-2025-6226
Preprint. Discussion started: 4 January 2026

Data availability

All raw data can be provided by the corresponding authors upon request.

Author contributions

DQ, HV, EL, and JPV planned the campaign; HV, DQ, BB, GL, FL, AS, AM, JM, and JPV performed the measurements; HV, DQ, FL, GS, DP, BG, HL, AR, MK, FW, CB, and JPV analyzed the data; HV and JPV wrote the manuscript draft; DQ, BB, EL, FL, NR, HL, SF, FW, ND, MC, GB, MJ, MA, JPV, and ND reviewed and edited the manuscript.

Acknowledgments

This research was funded by the NASA Upper Atmospheric Observation Composition (UACO) program and the Atmospheric Composition Modeling and Analysis Program (ACMAP). Additional support was provided by the Agence Nationale de la Recherche (ANR) through grant ANR-LABX-100-01 from Labex VOLTAIRE, managed by the University of Orleans. We thank Amit K. Pandit and Johnny Mau for their invaluable technical assistance in preparing the balloon campaign. We are grateful to Yunqian Zhu and Xinyue Wang for their insightful discussions and contributions to WACCM simulations.

Competing interests

At least one of the (co-)authors is a member of the editorial board of Atmospheric Chemistry and Physics.

https://doi.org/10.5194/egusphere-2025-6226
Preprint. Discussion started: 4 January 2026

References:

Allen, A. G., Baxter, P. J., and Ottley, C. J.: Gas and particle emissions from Soufrière Hills Volcano, Montserrat, West Indies: characterization and health hazard assessment, Bull. Volcanol., 62, 8–19, 2000.

Asher, E., Todt, M., Rosenlof, K., Thornberry, T., et al.: Unexpectedly rapid aerosol formation in the Hunga Tonga plume, Proc. Natl. Acad. Sci. U.S.A., 120, e2219547120, https://doi.org/10.1073/pnas.2219547120, 2023.

Ayris, P. M. and Delmelle, P.: The immediate environmental effects of tephra emission, Bull. Volcanol., 74, 1905–1936, https://doi.org/10.1007/s00445-012-0654-5, 2012.

Barbaro, E., et al.: Supplement of Chemical characterization of atmospheric aerosols at a high-altitude mountain site: a study of source apportionment, Atmos. Chem. Phys., 24, 2821–2835, https://doi.org/10.5194/acp-24-2821-2024-supplement, 2024.

Baron, A., Chazette, P., Khaykin, S., Payen, G., Marquestaut, N., Bègue, N., and Duflot, V.: Early evolution of the stratospheric aerosol plume following the 2022 Hunga Tonga–Hunga Ha'apai eruption: Lidar observations from Reunion (21° S, 55° E), Geophys. Res. Lett., 50, e2022GL101751, https://doi.org/10.1029/2022GL101751, 2023.

Duchamp, C., Legras, B., Podglajen, A., Sellitto, P., Bourassa, A. E., Rozanov, A., Taha, G., and Zawada, D. J.: Aerosol Composition and Extinction of the 2022 Hunga Plume Using CALIOP, EGUsphere, https://doi.org/10.5194/egusphere-2025-3355, 2025.

Evan, S., et al.: Rapid ozone depletion after humidification of the stratosphere by the Hunga Tonga Eruption, Science, 382, eadg2551, https://doi.org/10.1126/science.adg2551, 2023.

Ilyinskaya, E., Schmidt, A., Mather, T. A., Pope, F. D., Witham, C., Baxter, P., Jóhannsson, T., Pfeffer, M., Barsotti, S., Singh, A., Sanderson, P., Bergsson, B., McCormick Kilbride, B., Donovan, A., Peters, N., Oppenheimer, C., and Edmonds, M.: Understanding the environmental impacts of large fissure eruptions: Aerosol and gas emissions from the 2014–2015 Holuhraun eruption (Iceland), Earth Planet. Sc. Lett., 472, 309–322, https://doi.org/10.1016/j.epsl.2017.05.025, 2017.

Jenkins, S., Smith, C., Allen, M., and Grainger, R.: Tonga eruption increases chance of temporary surface temperature anomaly above 1.5 °C, Nat. Clim. Change, 13, 127–129, https://doi.org/10.1038/s41558-022-01568-2, 2023.

https://doi.org/10.5194/egusphere-2025-6226
Preprint. Discussion started: 4 January 2026

Khaykin, S., et al.: Global perturbation of stratospheric water and aerosol burden by Hunga eruption, Commun. Earth Environ., 3, 1–15, 2022.

Kovilakam, M., Thomason, L., and Knepp, T.: SAGE III/ISS aerosol/cloud categorization and its impact on GloSSAC, Atmos. Meas. Tech., 16, 2709–2731, https://doi.org/10.5194/amt-16-2709-2023, 2023.

Legras, B., Duchamp, C., Sellitto, P., Podglajen, A., Carboni, E., Siddans, R., Grooß, J.-U., Khaykin, S., and Ploeger, F.: The evolution and dynamics of the Hunga Tonga–Hunga Ha'apai sulfate aerosol plume in the stratosphere, Atmos. Chem. Phys., 22, 14957–14970, https://doi.org/10.5194/acp-22-14957-2022, 2022.

Millán, L., et al.: The Hunga Tonga-Hunga Ha'apai hydration of the stratosphere, Geophys. Res. Lett., 49, e2022GL099381, https://doi.org/10.1029/2022GL099381, 2022.

Millero, F. J., Feistel, R., Wright, D. G., and McDougall, T. J.: The composition of Standard Seawater and the definition of the Reference-Composition Salinity Scale, Deep Sea Res. Pt. I, 55, 50–72, https://doi.org/10.1016/j.dsr.2007.10.001, 2008.

Murphy, D. M., Froyd, K. D., Bian, H., Brock, C., Dibb, J., DiGangi, J., Diskin, G., Dollner, M., Kupc, A., Scheuer, E., Schill, G., Weinzierl, B., Williamson, C., and Yu, P.: The distribution of sea-salt aerosol in the global troposphere, Atmos. Chem. Phys. Discuss., 1–27, https://doi.org/10.5194/acp-2018-1013, 2018.

Nozaki, Y.: Elemental composition of seawater, in: Treatise on Geochemistry, 2nd Edn., edited by: Holland, H. D. and Turekian, K. K., Elsevier, Oxford, 2010.

Parker, D., Wilson, H., Jones, P. D., Christy, J. R., and Folland, C. K.: The impact of Mount Pinatubo World-Wide Temperatures, Int. J. Climatol., 16, 487–497, 1996.

Proud, S. R., Prata, A. J., and Schmauss, S.: The January 2022 eruption of Hunga Tonga-Hunga Ha'apai volcano reached the mesosphere, Earth Space Sci. Open Arch., https://doi.org/10.1002/essoar.10511092.1, 2022.

Robock, A.: Volcanic eruptions and climate, Rev. Geophys., 38, 191–219, https://doi.org/10.1029/1998RG000054, 2000.

Savarino, J., Bekki, S., Cole-Dai, J., and Thiemens, M. H.: Evidence from sulfate mass independent oxygen isotopic compositions of dramatic changes in atmospheric oxidation following massive volcanic eruptions, J. Geophys. Res.-Atmos., 108, 4671, https://doi.org/10.1029/2003JD003673, 2003.

https://doi.org/10.5194/egusphere-2025-6226
Preprint. Discussion started: 4 January 2026

709 Sellitto, P., Podglajen, A., Belhadji, R., et al.: The unexpected radiative impact of the Hunga
710 Tonga eruption of 15 January 2022, Commun. Earth Environ., 3, 288,
711 https://doi.org/10.1038/s43247-022-00618-z, 2022.
712 Schoeberl, M. R., Wang, Y., Ueyama, R., Dessler, A., Taha, G., and Yu, W.: The Estimated
713 Climate Impact of the Hunga Tonga-Hunga Ha'apai Eruption Plume, Geophys. Res. Lett.,
714 50, e2023GL104634, https://doi.org/10.1029/2023GL104634, 2023.
715 Stenchikov, G., Robock, A., Ramaswamy, V., Schwarzkopf, M. D., Hamilton, K., and
716 Ramachandran, S.: Arctic Oscillation response to the 1991 Mount Pinatubo eruption:
717 Effects of volcanic aerosols and ozone depletion, J. Geophys. Res., 107, 4803,
718 https://doi.org/10.1029/2001JD001255, 2002.
719 Stumm, W. and Morgan, J. J.: Aquatic Chemistry: Chemical Equilibria and Rates in Natural
720 Waters, 3rd Edn., John Wiley & Sons, 2012.
721 Sun, W. Y., Wang, B., Liu, J., Chen, D. L., Gao, C. C., Ning, L., and Chen, L.: How northern
722 high-latitude volcanic eruptions in different seasons affect ENSO, J. Climate, 32, 3245–
723 3262, 2019.
724 Taha, G., Loughman, R., Colarco, P. R., Zhu, T., Thomason, L. W., and Jaross, G.: Tracking the
725 2022 Hunga Tonga–Hunga Ha'apai aerosol cloud in the upper and middle stratosphere
726 using space-based observations, Geophys. Res. Lett., 49, e2022GL10009,
727 https://doi.org/10.1029/2022GL10009, 2022.
728 Thomason, L. W., Rieger, L. A., and Millán, L. F.: Global satellite observations of stratospheric
729 aerosols: A review, Rev. Geophys., 56, 692–726, https://doi.org/10.1029/2017RG000579,
730 2018.
731 Vernier, J.-P., Thomason, L. W., Pommereau, J.-P., Bourassa, A., Pelon, J., Garnier, A.,
732 Hauchecorne, A., Trepte, C., Degenstein, D., and Vargas, F.: Major influence of tropical
733 volcanic eruptions on the stratospheric aerosol layer during the last decade, Atmos.
734 Chem. Phys., 15, 3525–3542, https://doi.org/10.5194/acp-15-3525-2015, 2015.
735 Zhao, Y., Zhao, C., and Leinen, M.: Depletion of atmospheric nitrate and chloride as a
736 consequence of the Toba volcanic eruption, Geophys. Res. Lett., 23, 2513–2516,
737 https://doi.org/10.1029/96GL02201, 1996.

https://doi.org/10.5194/egusphere-2025-6226
Preprint. Discussion started: 4 January 2026

738 Zhu, Y., Bardeen, C. G., Tilmes, S., et al.: Perturbations in stratospheric aerosol evolution due to
739 the water-rich plume of the 2022 Hunga-Tonga eruption, Commun. Earth Environ., 3,
740 248, https://doi.org/10.1038/s43247-022-00575-7, 2022.
741 Zuo, M., et al.: Volcanoes and climate: Sizing up the impact of the recent Hunga Tonga-Hunga
742 Ha'apai volcanic eruption from a historical perspective, Adv. Atmos. Sci., 39, 1986–
743 1993, 2022.
744
745